Complex network analysis of the gravity effect on premixed flames propagating in a Hele-Shaw cell

Yuji Nomi ⬤, Hiroshi Gotoda ⬤,[*] and Shuya Kandani ⬤

Department of Mechanical Engineering, Tokyo University of Science, 6-3-1 Niijuku, Katsushika, Tokyo 125-8585, Japan

Christophe Almarcha ⬤

Aix-Marseille University, CNRS, Centrale Marseille, IRPHE, F-13451 Marseille Cedex 20, France

We study the effect of gravity on spatiotemporal flame front dynamics in a Hele-Shaw cell from the viewpoint of complex networks. The randomness in flame front dynamics significantly increases with the gravitational level when the normalized Rayleigh number R_a is negative. This is clearly identified by two network entropies: the flame front network entropy and the transition network entropy. The irregular formation of large-scale wrinkles driven by the Rayleigh-Taylor instability plays an important role in the formation of high-dimensional deterministic chaos at $R_a < 0$, resulting in the increase in the randomness of flame front dynamics.

I. INTRODUCTION

A chemically reacting interfacial phenomenon with a high temperature field, which is referred to as combustion, is one of the well-known complex dissipation phenomena. Intrinsic instabilities owing to the thermal-diffusive effect [1,2] and/or hydrodynamic Darrieus-Landau-type effect [3] give rise to significant deformation of an initially planar flame, leading to the self-turbulization of the flame front. The elucidation and characterization of flame front dynamics have long been an important subject of theoretical and numerical studies in combustion physics and related branches of nonlinear science. Intrinsic instabilities can be modeled by nonlinear evolution equations such as the Sivashinsky equations [4], and the importance of nonlinear evolution equations has been shown in many studies [4–8]. A simple geometry with a narrow gap between two parallel plates, known as the Hele-Shaw cell, is an interesting apparatus for use in the elucidation of flame front dynamics induced by intrinsic instabilities in a quasi-two-dimensional system. Almarcha *et al.* [9] have recently demonstrated that the Michelson-Sivashinsky equation can explain the flame dynamics, pole trajectories, and cell size statistics experimentally obtained using a Hele-Shaw burner.

Network science incorporating the conceptional framework from graph theory based on discrete mathematics has recently allowed us to seek universal organizing principles in complex systems [10]. Taira *et al.* [11] studied the relevance of the network science to turbulent and vortical flow systems, which importantly brings about disciplinary fusion between fluid dynamics and network science. The importance of the network science in turbulent flow research has been highlighted in some review articles [12,13]. Diverse transformation methodologies from time series to network or graph topologies (e.g., visibility graphs [14,15], recur-

rence networks [16], and cycle networks [17]) are widely recognized in the nonlinear science community. The resulting network representations have recently been adopted for complex combustion dynamics in various thermoacoustic systems [18–22]. For physical settings different from those in the above studies [18–20,22], Gotoda and co-workers have clarified the scale-free structure in flame front fluctuations in a diffusion flame induced by radiative heat loss [23] using natural and horizontal visibility graphs and in a rotating premixed flame [24] using the recurrence network. They have also clearly shown that network entropies in a recurrence network and the horizontal visibility graph are useful for quantifying the changes in the randomness of dynamical states from low-dimensional chaos to high-dimensional chaos in a buoyancy-driven turbulent fire [25,26]. In addition to those networks [14–17], the ordinal partition transition network [27,28] incorporating the concept of symbolic dynamics has very recently been shown to ensure good performance in characterizing the dynamical behavior during thermoacoustic combustion oscillations, including the detection of the state transition from a practical application perspective [29]. The findings obtained in those studies [18–26,29] have changed our overall understanding and interpretation of nonlinear dynamics in combustion phenomena, providing interdisciplinary platforms for nonlinear time series analysis. Our interest in this study is to examine whether the information entropy in the network topologies has potential use in discussing the complexity of flame front dynamics in a Hele-Shaw cell.

A large density difference in the interface between hot combustion products and cold unburnt reactants subjected to gravity can trigger a buoyant force. This results in a significant deformation of flame front associated with the Rayleigh-Taylor instability mechanism. The main purpose of this study is to elucidate how the gravitational level alters the randomness in the spatiotemporal flame front dynamics in a Hele-Shaw cell from the viewpoint of complex networks. The outline of this paper is as follows. In Sec. II, we present

the derivation of a nonlinear evolution equation modeling flame front dynamics in a Hele-Shaw cell. In Sec. III, we provide a mathematical treatment of complex-network-based approaches. Numerical results obtained using the nonlinear evolution equation are presented in Sec. IV. We give our main conclusions in Sec. V.

II. NONLINEAR EVOLUTION EQUATIONS AND NUMERICAL COMPUTATION

For the derivation of a nonlinear evolution equation describing flame front dynamics in a Hele-Shaw cell, we first consider the following two-dimensional G-equation [30]:

$$\frac{\partial G}{\partial t} + \mathbf{v_b} \cdot \nabla G = \|\nabla G\|. \tag{1}$$

Here, $G(x, z, t)$ represents the reacting scalar field, x and z are the dimensionless space coordinates normalized by the laminar flame thickness δ_L, $\mathbf{v_b} = (u_b, w_b)$, and t is the dimensionless time ($= \delta_L/S_L^b$), where S_L^b is the laminar burning velocity in the burnt gas region. The entire flow field consists of two regions: $G > G_0$ is the region of hot combustion products and $G < G_0$ is the region of cold reactants [30], where G_0 is an isoscalar surface. In this study, we define the flame front displacement $h(x, t)$ [30] as

$$G(x, z, t) - G_0 = z - h(x, t). \tag{2}$$

Equation (3) is obtained by substituting Eq. (2) into Eq. (1):

$$\frac{\partial h}{\partial t} + \frac{1}{2}\left(\frac{\partial h}{\partial x}\right)^2 = w_b - 1 - u_b\frac{\partial h}{\partial x}. \tag{3}$$

In accordance with a previous study [31], we introduce the following scaled variables:

$$u_b = \gamma^2 U_b, \quad w_b = 1 + \gamma^2 W_b,$$
$$h = \gamma H, \quad t = \tau/\gamma. \tag{4}$$

Here, γ ($= 1 - \rho_b/\rho_u$) is a dimensionless parameter characterizing thermal expansion across the flame front, and ρ_b (respectively, ρ_u) is the density of hot combustion products (respectively, cold reactants).

Equation (3) can then be written as

$$\frac{\partial H}{\partial \tau} + \frac{1}{2}\left(\frac{\partial H}{\partial x}\right)^2 = W_b - \gamma U_b\frac{\partial H}{\partial x}. \tag{5}$$

Equation (7) is derived by adopting the zeroth order of Eq. (6) for H, U_b, and W_b in Eq. (5). Note that we neglect $U_b\partial H/\partial x$ by considering the zeroth-order approximation since the flow in a Hele-Shaw cell is irrotational. A form similar to Eq. (7) has been obtained in different combustion settings [31–35].

$$H = H^{(0)} + \gamma H^{(1)} + O(\gamma^2),$$
$$U_b = U_b^{(0)} + \gamma U_b^{(1)} + O(\gamma^2),$$
$$W_b = W_b^{(0)} + \gamma W_b^{(1)} + O(\gamma^2), \tag{6}$$

$$\frac{\partial H}{\partial \tau} + \frac{1}{2}\left(\frac{\partial H}{\partial x}\right)^2 = W_b. \tag{7}$$

Following the procedure of a previous study [36], we introduce Eq. (8) for the stream function $\Phi(x, z, \tau)$ incorporating Darcy's law to deal with the fluid flow in a Hele-Shaw cell [37,38]:

$$\nabla^2\Phi = -R\frac{\partial H}{\partial x}\delta(z - H). \tag{8}$$

Here, $R = g\gamma/12$, g is the dimensionless acceleration of gravity normalized by $\nu S_L^b/d^2$, d is the gap width between two vertical walls, ν is the kinematic viscosity of combustion products, and δ is the delta function.

We obtain Eq. (9) by substituting $W_b = \partial\Phi/\partial x$ into Eq. (7):

$$\frac{\partial H}{\partial \tau} + \frac{1}{2}\left(\frac{\partial H}{\partial x}\right)^2 = \frac{\partial \Phi}{\partial x}. \tag{9}$$

Sivashinsky [4] proposed a nonlinear evolution equation incorporating the thermal-diffusive effect on flame front instability, which is considered in this study.

$$\frac{\partial H}{\partial \tau} + \varepsilon\frac{\partial^2 H}{\partial x^2} + 4\frac{\partial^4 H}{\partial x^4} = 0. \tag{10}$$

Here, $\varepsilon = (L_{e0} - L_e)/(1 - L_{e0})$, L_e is the Lewis number of the cold reactants, and L_{e0} is the critical Lewis number.

As in previous studies [31–33,35], we obtain Eq. (11) by the synthesis of Eqs. (9) and (10) in this study. The coefficient of $\partial H/\partial \tau$ in Eq. (9) is set to 1, as in the previous studies [31–33,35].

$$\frac{\partial H}{\partial \tau} + \frac{1}{2}\left(\frac{\partial H}{\partial x}\right)^2 + \varepsilon\frac{\partial^2 H}{\partial x^2} + 4\frac{\partial^4 H}{\partial x^4} = \frac{\partial \Phi}{\partial x}. \tag{11}$$

In accordance with a previous study [39], we obtain the nonlinear evolution describing flame front dynamics in a Hele-Shaw cell after considering a similar variable conversion into Eqs. (8) and (11).

$$\frac{\partial H}{\partial \tau} + \frac{1}{2}\left(\frac{\partial H}{\partial x}\right)^2 + \bar{\nu}\frac{\partial^2 H}{\partial x^2} + \frac{\partial^4 H}{\partial x^4} = \frac{\partial \Phi}{\partial x}\Big|_{z=H},$$
$$\frac{\partial^2 \Phi}{\partial x^2} + \beta^2\frac{\partial^2 \Phi}{\partial z^2} = -\beta R_a\frac{\partial H}{\partial x}\delta(z - H). \tag{12}$$

Here, H is the flame front fluctuations, R_a ($= g\gamma/(6\sqrt{\varepsilon})$) is the normalized Rayleigh number, $\beta = 2/\sqrt{|\varepsilon|^3}$, and $\bar{\nu} = \varepsilon/|\varepsilon|$. $\bar{\nu}$ is either positive or negative depending on the sign of ε. The thermal-diffusive effect is dominant at $\bar{\nu} > 0$, whereas it is suppressed at $\bar{\nu} < 0$. We set $\bar{\nu}$ to 1 in this study.

We finally obtain Eq. (13) by introducing a Fourier series to $H(x, \tau)$ and $\Phi(x, \tau)$ under the periodic boundary condition:

$$\frac{\partial H}{\partial \tau} + \frac{1}{2}\left(\frac{\partial H}{\partial x}\right)^2 + \bar{\nu}\frac{\partial^2 H}{\partial x^2} + \frac{\partial^4 H}{\partial x^4}$$
$$+ \frac{R_a}{2}\sum_{k=-\infty}^{\infty} k H_k \cos kx = 0. \tag{13}$$

When R_a is positive (negative), the flame front propagates downwardly (upwardly). The gravitational effect stabilizes (destabilizes) flame wrinkling in positive (negative) gravity with $R_a > 0$ ($R_a < 0$).

In this study, the computational domain with the system size $L = 100$ is discretized into $N_L = 500$ points. Equation

(13) is numerically solved by adopting a pseudospectral method for spatial derivatives that uses the fast Fourier transform to transform the $H(x, \tau)$ solution to Fourier space with wave number $k \in [-\pi/\Delta x, \pi/\Delta x]$, where $\Delta x = L/N_L$. The nonlinear term is evaluated in real space and transformed back to Fourier space using the inverse fast Fourier transform. As in a previous study [40], the solution is propagated in time using a modified fourth-order exponential time-differencing–time-stepping Runge-Kutta scheme [41] with time step $\Delta\tau = 0.01$ and sampling time interval $d\tau = 1$. Note that Figs. 3, 7, and 13 were obtained after averaging over 10 different realizations of the initial conditions.

III. COMPLEX-NETWORK-BASED ANALYTICAL METHODS

As mentioned in Sec. I, we employ two networks in this study: the ordinal partition transition network and the flame front network based on the natural visibility graph. The central idea of these networks is described here.

A. Ordinal partition transition network

The ordinal partition transition network based on the Markov chain, which incorporates the concept of symbolic dynamics, was proposed by Small and McCullough *et al.* [27,28]. For the construction of the network, the local temporal evolution of flame front fluctuations $\mathbf{H} = (H(\tau), H(\tau+1), ..., H(\tau+D-1))$ at $x = 0$ is mapped into symbolic transition patterns, where D corresponds to the rank order pattern length. The nodes in the network are represented by each permutation pattern π_i $(i = 1, 2, ..., D!)$. The links between the nodes are expressed by the transfer probability w_{ij} $(= p(\Gamma_{ij}))$ from the ith- to the jth-order pattern in a time series, where $\Gamma_{ij} = \pi_i \rightarrow \pi_j$. We do not overlap the successive partitions in a time series. After considering w_{ij} between π_i and π_j for the definition of the information entropy, we estimate the transition network entropy S_t in the network as

$$S_t = -\frac{\sum_{i=1}^{D!} \sum_{j=1}^{D!} w_{ij} \ln w_{ij}}{\ln D!^2}. \tag{14}$$

For the estimation of S_t, D is set to 3 in this study. The permutation entropy [42], which is the information entropy considering the probability distribution of possible existing rank order patterns in a time series, can quantify the randomness of dynamic behaviors. The transition network entropy is superior to the permutation entropy in the sense that the dynamical transition of the rank order patterns is considered in the ordinal partition transition network.

The distinction between chaotic and stochastic states is an intriguing challenge in a nonlinear time series analysis. The permutation spectrum test [43] is useful for examining the presence of deterministic chaos in terms of symbolic dynamics and has been widely used for various physical settings from fluid to combustion phenomena [24,26,29,40,44]. The central idea of this test is that if the dynamic behavior is dominated by a deterministic process, forbidden patterns appear in the permutation spectrum. Note that the permutation spectrum consists of the frequency distribution of the permutation pattern for each sequence in disjointed windows and

their standard deviation. We adopt this idea for the forbidden transition patterns in the ordinal partition transition network to distinguish between chaotic and stochastic states; this has also more recently been discussed by Olivares *et al.* [45]. We here show the validity of the permutation transition spectrum test, focusing on Lorenz chaos and two important stochastic fluctuations: white Gaussian noise and Brownian motion.

Figure 1 shows the permutation transition spectrum for Lorenz chaos, white Gaussian noise, and Brownian motion, together with representative network structures. Forbidden transition patterns appear for Lorenz chaos, whereas the number of forbidden patterns is zero for both Gaussian noise and Brownian motion. This clearly shows that the permutation transition spectrum test enables us to distinguish between chaotic and stochastic states. On this basis, we estimate the number of forbidden transition patterns N_{ft} normalized by the maximum number of possible forbidden transition patterns $(= D!^2)$ in the ordinal partition transition network.

B. Flame front network

The flame front network, which is constructed directly from the flame front configuration, has recently been proposed by Singh *et al.* [21]. They clearly showed that the degree distribution in the network is an important network property for characterizing the flame-turbulence interaction. The flame front network is obtained by adopting the visibility algorithm [14] for flame front positions. The node v_i in the network corresponds to flame front position, and two nodes v_i and v_j are connected by links under the following geometrical criterion. If the flame front does not exist on the two-dimensional line of sight from v_i to v_j, v_i will be considered as being visible to v_j. The adjacency matrix $A_{ij} = 1$ if v_i is visible to v_j; otherwise, $A_{ij} = 0$. We obtain the flame front network entropy by estimating the degree k_i $(= \sum_j A_{ij})$ in the network.

$$h_n = -\sum_{k=1}^{k_{\max}} p(k) \ln p(k). \tag{15}$$

Here, h_n is the flame front network entropy, $p(k)$ is the probability of the degree k in the network, and $k_{\max}$ is the maximum k.

IV. RESULTS AND DISCUSSION

Figure 2 shows the spatiotemporal structure and extracted spatial variation in H for different R_a. The flame front is significantly wrinkled at $R_a = 0$, and well-organized intrinsic cells with small scales are formed throughout the flame front. We clearly observe arrayed structures with large fluctuations due to the continuous interactions between the cells. The amplitude of H at $R_a > 0$ decreases owing to the stabilizing gravitational effect, accompanying with the local formation of regular structures. In contrast, at $R_a < 0$, complex dynamics are progressively promoted owing to the destabilization of the arrayed structures, yielding wrinkles with substantial amplitude and large-scale wavelength. Figure 3 shows h_n as a function of R_a. h_n at $R_a > 0$ $(R_a < 0)$ decreases (increases) with increasing g, indicating a decrease (increase) in the randomness of the flame front configuration. The gradient of
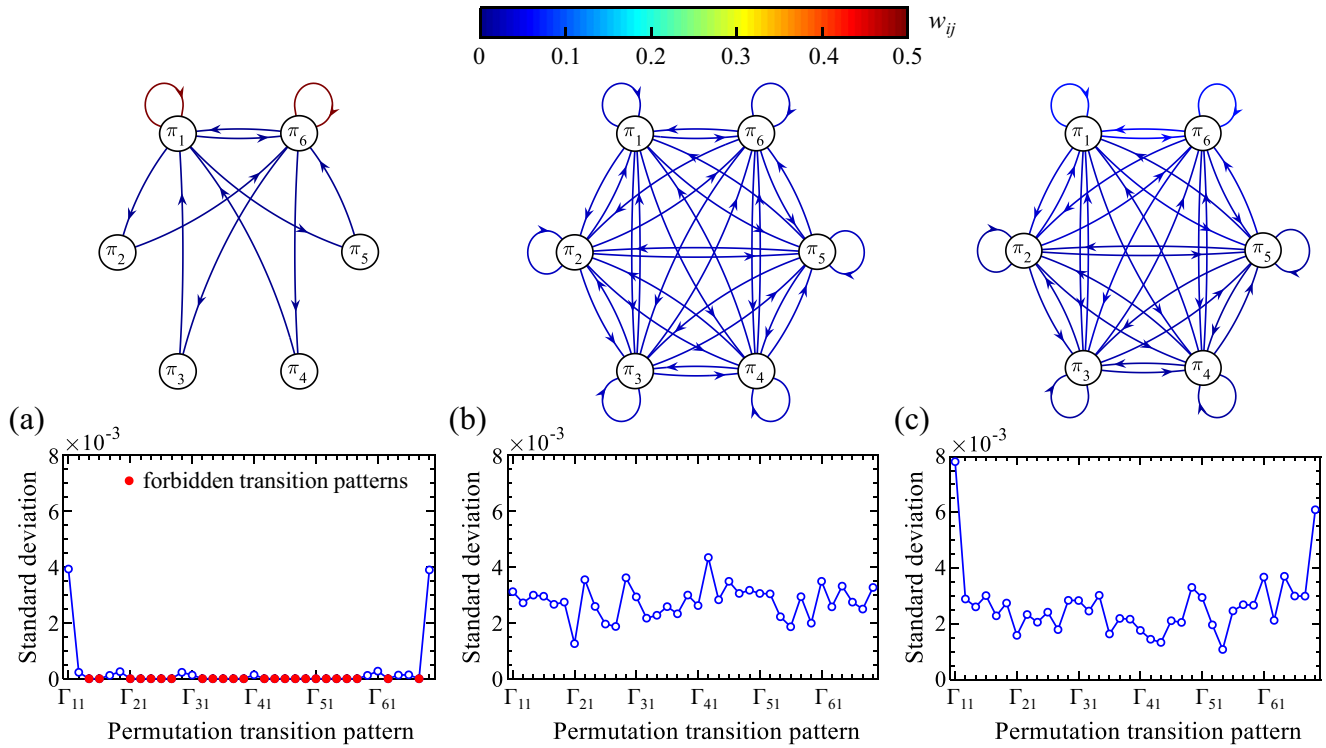
FIG. 1. Permutation transition spectrum for (a) Lorenz chaos, (b) white Gaussian noise, and (c) Brownian motion, together with representative network structures.

h_n with respect to R_a at $R_a < 0$ is larger than that at $R_a > 0$. The promotion of the Rayleigh-Taylor instability at $R_a < 0$ gives rise to a wider range of degree distributions in the network, resulting in a notable increase in flame front network entropy. The normalized Rayleigh number more strongly affects the complexity of an upwardly propagating flame front configuration than that of a downwardly propagating flame.

The local temporal evolution of H at $x = 0$ and the corresponding power spectrum density (PSD) are shown in Fig. 4 for different R_a. Aperiodic fluctuations of H are formed at $R_a = 0$, exhibiting exponential power-law decay in the PSD. The exponential power-law decay indicates the presence of chaotic dynamics. The irregularity of H becomes small (large) at $R_a = 1$ ($R_a = -2$). The PSD at $R_a = -2$ exhibits power-law decay with the exponent $\kappa \sim -5/3$, indicating
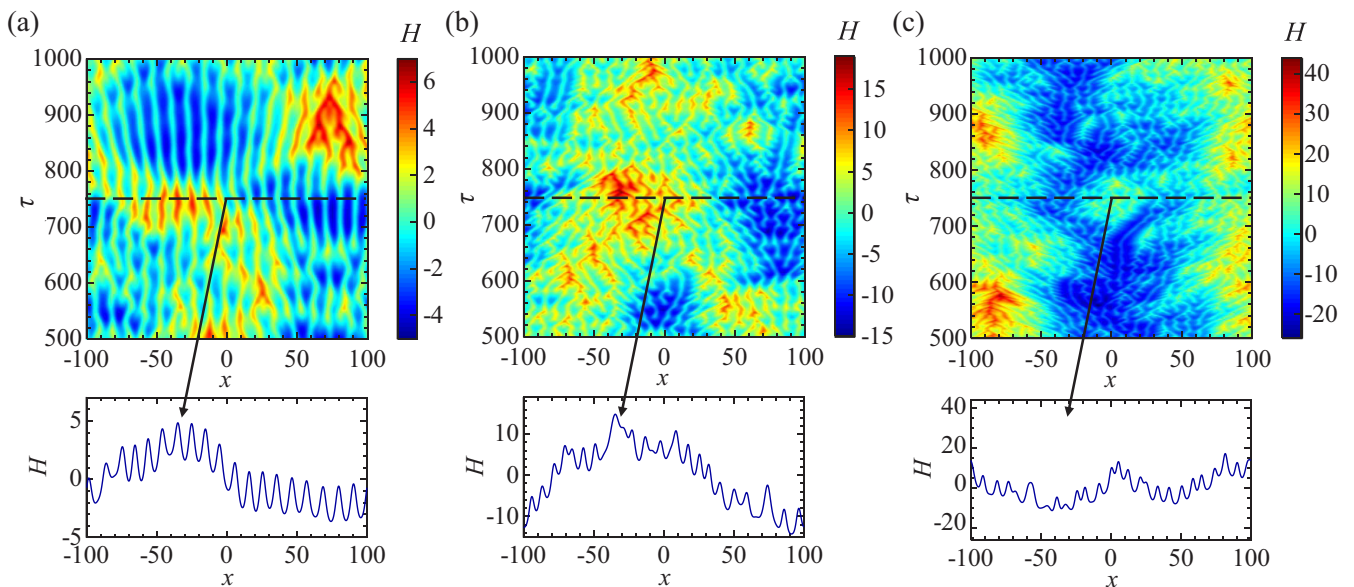

FIG. 2. Spatiotemporal structure and extracted spatial variation in flame front fluctuations H for different normalized Rayleigh numbers R_a. (a) $R_a = 1$, (b) $R_a = 0$, and (c) $R_a = -1$.
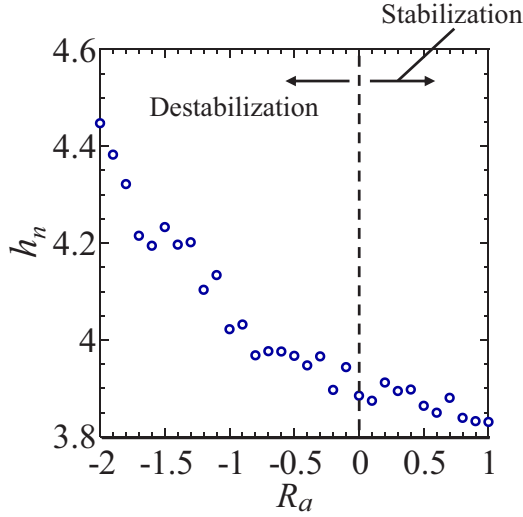
FIG. 3. Variation in flame front network entropy h_n as a function of normalized Rayleigh number R_a.

the presence of chaos with typical turbulentlike dynamics. Figure 5 shows the permutation transition spectrum at $R_a = 0$, together with a representative network structure. We observe two specific self-loop transition patterns Γ_{11} and Γ_{66}, where $\Gamma_{11}(\Gamma_{66}) = \pi_1 \rightarrow \pi_1$ ($\pi_6 \rightarrow \pi_6$). They correspond to the monotonically increasing and decreasing processes, respectively. Some forbidden transition patterns (unconnected nodes) appear in the network. This clearly shows the appearance of nonlinear determinism, indicating that the dynamic behavior of H is chaotic. The iterative amplitude-adjusted Fourier transform (IAAFT) surrogate data method [46] is a well-known statistical test for examining nonlinear determinism in a time series. The null hypothesis of IAAFT surrogate data is that the irregular components of a time series are governed by a Gaussian linear stochastic process. We here examine the frequency distribution of the forbidden transition pattern numbers and the transition network entropy for the original and surrogate data at $R_a = -1$ as a representative case of chaotic fluctuations. Figure 6 shows the frequency distributions of N_{ft} and S_t for the original and surrogate data, where S_t is the transition network entropy. Note that 500 sets of surrogate data are considered in this study. The values of N_{ft} and S_t for the original data do not correspond to those for the surrogate data. The hypothesis can be rejected with 95% reliability obtained by a t test of estimates of N_{ft} and S_t for the surrogate data sets. This indicates the possible presence of a nonlinear deterministic process. Variations in N_{ft} and S_t are shown in Fig. 7 as a function of R_a. N_{ft} (S_t) significantly increases (decreases) with increasing g under $R_a > 0$. The formations of Γ_{11} and Γ_{66} become predominant, resulting in a significant decrease in S_t. In contrast, N_{ft} (S_t) significantly decreases (increases) with increasing g under $R_a < 0$, which indicates an increase in the randomness of flame front dynamics.

In relation to symbolic dynamics, the multiscale complexity-entropy causality plane (CECP) is also useful for verifying the presence of deterministic chaos in aperiodic fluctuations. The CECP consists of the permutation entropy
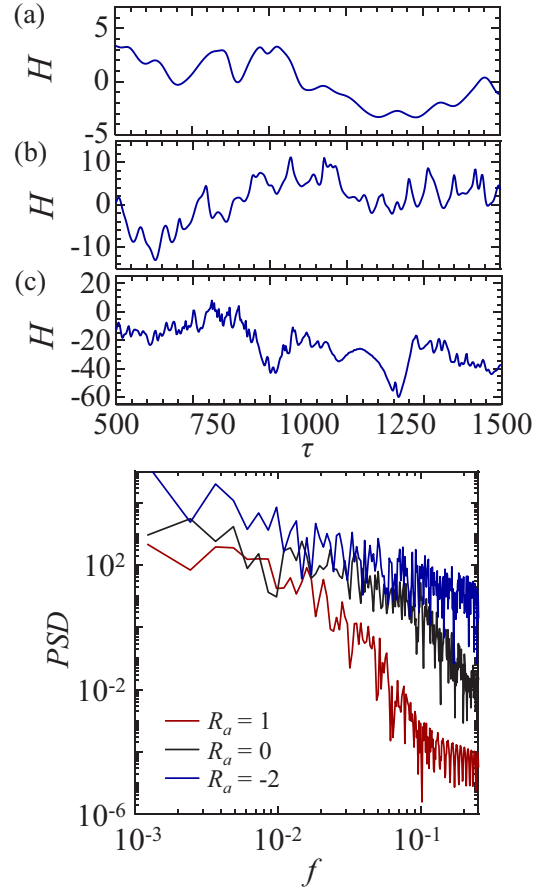

FIG. 4. Variations in local temporal evolution of flame front fluctuations H at location $x = 0$ and corresponding power spectrum density (PSD) for different normalized Rayleigh numbers R_a. (a) $R_a = 1$, (b) $R_a = 0$, and (c) $R_a = -2$.

S_p and the Jensen-Shannon complexity C_{JS}, and can quantify the degree of dynamical complexity at various time scales in phase space. We adopt the multiscale CECP for the temporal evolution of H (see Ref. [47] for details of the multiscale CECP). Figure 8 shows the variations in S_p and C_{JS} of H as a function of the embedding delay time τ_d in phase space for different R_a, together with the trajectory on the CECP. Here, the maximum and minimum of C_{JS} are $C_{JS,\max}$ and $C_{JS,\min}$, respectively. S_p at $R_a = 1$ monotonically increases with τ_d and becomes almost constant. C_{JS} takes a local maximum value at $\tau = 6$ and gradually decays with increasing τ_d. The trajectory on the CECP moves from $(S_p, C_{JS}) = (0.26, 0.22)$ to $(0.96, 0.07)$ with increasing τ_d, clearly exhibiting a parabolic curve. The shape of the trajectory at $R_a = 1$ almost corresponds to that of low-dimensional deterministic chaos obtained in the Lorenz system [48]. The Lorenz system describing the global dynamics of Rayleigh-Bénard convection is widely used to explain the nonlinear dynamics appearing in a buoyancy-driven irregular convective flow [49–52]. Although the Lorenz chaos does not represent the flame front dynamics in this study, on the basis of a finding by Zunino *et al.* [47] and Tang *et al.* [48], the complexity of flame front dynamics at $R_a = 1$ is equivalent to low-dimensional deterministic chaos. In contrast, S_p at $R_a = -1$ rapidly increases with τ_d,
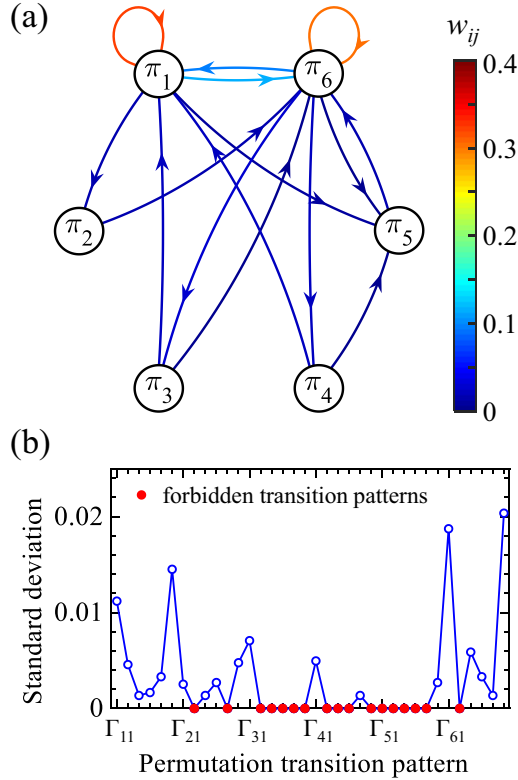
FIG. 5. (a) Representative network structure and (b) permutation transition spectrum at normalized Rayleigh number $R_a = 0$.

and the maximum value of C_{JS} is shifted at a lower τ_d. The left point of the trajectory on the CECP is located in the middle of the upper region. In our preliminary test using the Kuramoto-Sivashinsky equation, we observed that for high-dimensional chaos, the left-hand side of the curve on the CECP is located in the middle of the upper region of the plane. On this basis, it is conceivable that the flame front dynamics at $R_a = -1$ exhibits high-dimensional deterministic chaos.

A positive Lyapunov exponent is an important signature of chaos, which indicates an exponentially rapid divergence of neighboring trajectories in phase space. One of the standard methods of estimating the maximum Lyapunov exponent is the Rosenstein method [53]. We here estimate the largest Lyapunov exponent $\lambda_{\max}$ for H at $R_a = -1$ by the Rosenstein method. In this method, we assume that the pair of nearest neighbors along the trajectories in phase space consisting of $\mathbf{H}(\tau)$ develops exponentially and diverges at a certain rate after $\Delta\tau_l$ time. This rate corresponds to $\lambda_{\max}$ $(= d_R/\Delta\tau_l$, where $d_R = (1/N)\sum_{\tau=1}^{N} \ln|\mathbf{H}(\tau + \Delta\tau_l) - \mathbf{H}(\tau_i + \Delta\tau_l)|/|\mathbf{H}(\tau) - \mathbf{H}(\tau_i)|)$. $\lambda_{\max}$ is finally obtained from the slope of d_R plotted as a function of $\Delta\tau_l$. Figure 9 shows the variation in d_R as a function of $\Delta\tau_l$ for the original data of H at $R_a = -1$, together with the frequency distribution of $\lambda_{\max}$ for the original and surrogate data of H. Here, $N = 5000$. Five hundred sets of surrogate data are considered as well as the estimation of N_{ft} and S_t. We observe a monotonic increase in d_R with increasing $\Delta\tau_l$, indicating an exponential divergence of the distance between initially neighboring trajectories. As
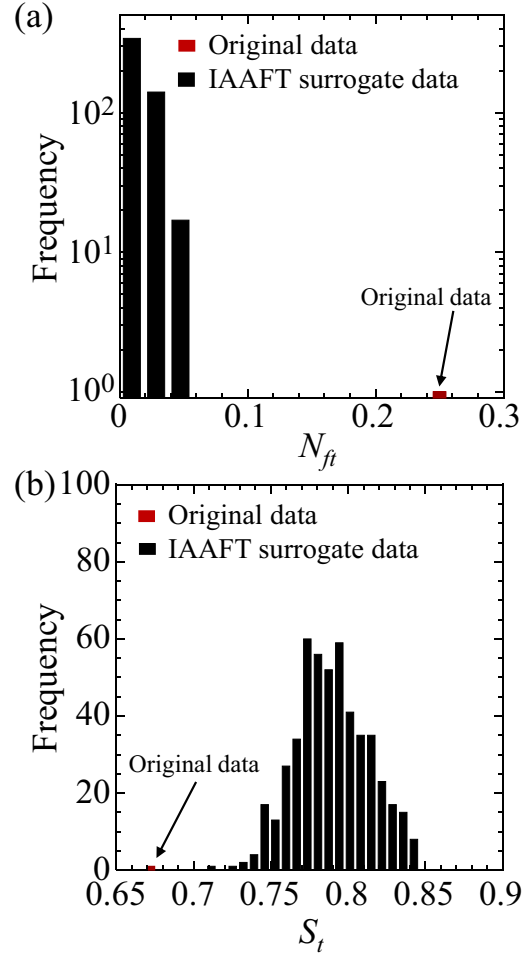

FIG. 6. Frequency distribution of (a) numbers of forbidden patterns in transition network N_{ft} and (b) transition network entropy S_t for original and surrogate data at normalized Rayleigh number $R_a = -1$.

shown by the dashed line, we estimate $\lambda_{\max}$ from the slope of d_R in terms of $\Delta\tau_l$. Here, the region of the slope for estimating $\lambda_{\max}$ is selected in accordance with a previous study [53]. In our preliminary test, we confirm that $\lambda_{\max}$ for the time series data of the Lorenz chaos is in agreement with that obtained by Rosenstein *et al.* [53] and Jayaraman *et al.* [54]. The value of $\lambda_{\max}$ at $R_a = -1$ is approximately 0.18 and is positive. As shown in Fig. 9(b), the value of $\lambda_{\max}$ for the original data does not correspond to those for the surrogate data, and the hypothesis can be rejected with 95% reliability obtained by a t test as well as on the basis of N_{ft} and S_t. This result clearly shows that the dynamic behavior of flame front instability is governed by a nonlinear deterministic process.

The short-term predictability and long-term unpredictability of dynamic behavior are important features of chaos in terms of orbital instability in phase space. Gotoda and co-workers [40,55,56] have proposed a methodology of nonlinear forecasting to distinguish between chaotic and stochastic states. Taking particular note of this feature, we adopt a nonlinear forecasting method for the temporal evolution of H (see [40,55,56] for details of the nonlinear forecasting method). In this method, the temporal evolution of
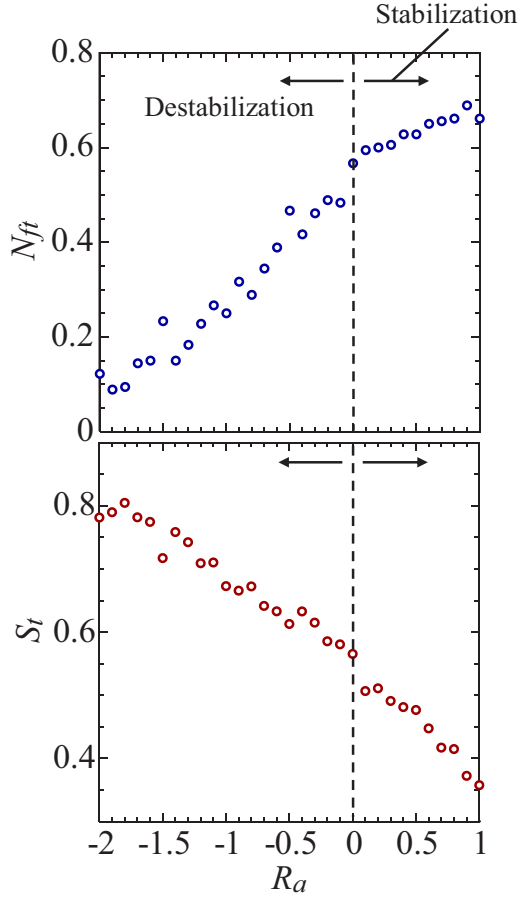
FIG. 7. Variations in (a) number of forbidden transition patterns N_{ft} and (b) transition network entropy S_t as a function of normalized Rayleigh number R_a.

FIG. 8. Variations in permutation entropy S_p and Jensen-Shannon complexity C_{JS} of H as a function of embedding delay time τ_d in phase space at normalized Rayleigh numbers (a) $R_a = 1$ and (b) $R_a = -1$, together with trajectory on multiscale complexity-entropy causality plane (CECP). Here, the two continuous parabolic lines represent $C_{JS,\max}$ and $C_{JS,\min}$.

the increments $\Delta H\ (= H(\tau + 1) - H(\tau))$ is first divided into two parts: one based on the library data and the other on the reference data set. After constructing a phase space from the library data, we obtain the predicted point $\Delta\hat{\mathbf{H}}(\tau_f + T)$ of a trajectory in the phase space. Here, $\Delta\hat{\mathbf{H}}(\tau_f + T) = \sum_{k=1}^{K} \Delta\mathbf{H}(\tau_k + T)\exp(-\|\Delta\mathbf{H}(\tau_f) - \Delta\mathbf{H}(\tau_k)\|)/\sum_{k=1}^{K}\exp(-\|\Delta\mathbf{H}(\tau_f) - \Delta\mathbf{H}(\tau_k)\|)$, $\Delta\mathbf{H}(\tau_k)$ is the point near a final point $\Delta\mathbf{H}(\tau_f)$ of a trajectory in phase space, T is the time step, and K is the number of nearby points. The temporal evolution of the predicted $\Delta\hat{H}(\tau_f + T)$ is finally obtained inversely from $\Delta\hat{\mathbf{H}}(\tau_f + T)$. We estimate the correlation coefficient C between the predicted $\Delta\hat{H}(\tau_f + T)$ and the reference $\Delta H(\tau_f + T)$. The short-term predictability and long-term unpredictability characteristics are determined by examining the relationship between C and the prediction time τ_p. Figure 10 shows the variation in C as a function of τ_p for different R_a. Note that $K = 50$ and ΔH at $500 < \tau \leqslant 3000$ are used as the library data, whereas those at $3000 < \tau \leqslant 5500$ are used as the reference data. When R_a is 0, C at $\tau_p = 1$ is approximately 0.93 with high predictability. It decreases exponentially with increasing τ_p, forming the region of short-term predictability and long-term unpredictability. This is a distinctive feature of deterministic chaos. When R_a is 1, C at $\tau_p = 1$ is approximately 0.98 and gradually
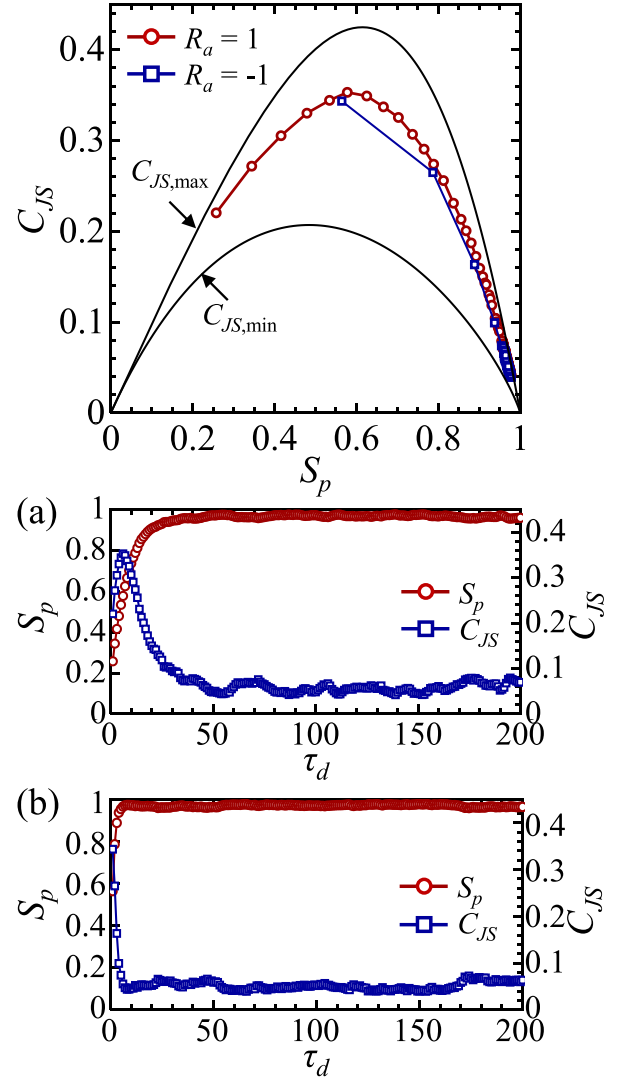
decreases with increasing τ_p. The short-term predictability region is significantly larger than that for $R_a = 0$. The important point to note here is that the distribution of C in terms of τ_p at $R_a = 1$ nearly corresponds to that for Lorenz chaos. This indicates that the dynamical state represents low-dimensional deterministic chaos. When $R_a = -1$, C rapidly decreases with increasing τ_p but does not take a value close to zero at $1 \leqslant \tau_p \leqslant 5$, clearly indicating that the flame front dynamics does not follow a stochastic process. The frequency distribution of C for the original and surrogate data of ΔH at $R_a = -1$ is shown in Fig. 11. Note that we analyze the original and 500 sets of surrogate data at $\tau_p = 1$ corresponding to the short-term predictability region. The value of C for the original data does not correspond to those for the surrogate data, which clearly indicates the presence of a nonlinear deterministic process. The results shown
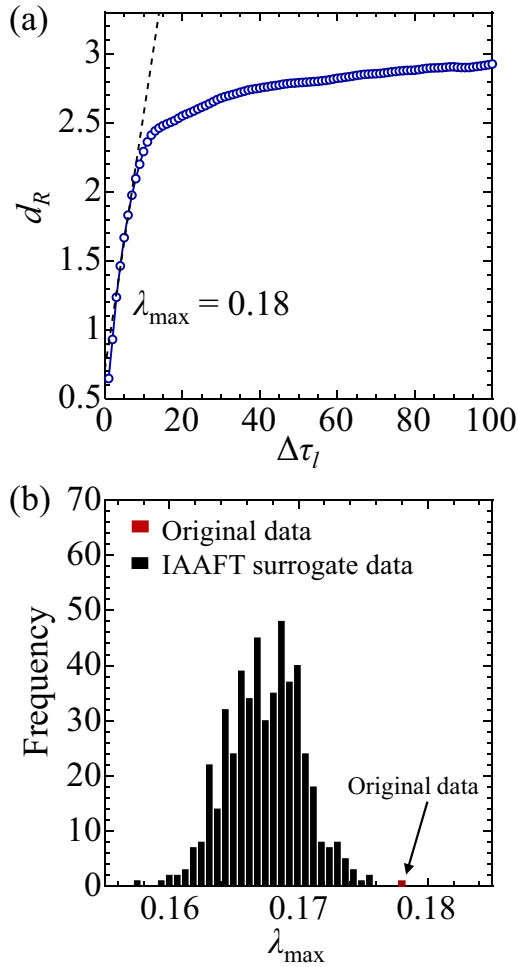
FIG. 9. (a) Variation in d_R as a function of $\Delta\tau_l$ for original data of H at normalized Rayleigh number $R_a = -1$, together with (b) frequency distribution of $\lambda_{\max}$ for original and surrogate data of H.
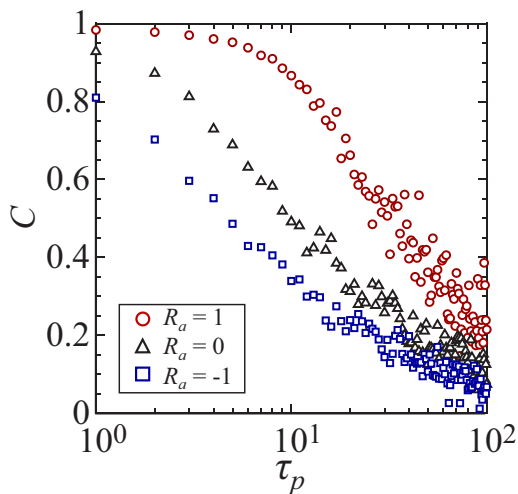

FIG. 10. Variation in correlation coefficient C between actual and predicted temporal evolutions for increments ΔH as a function of prediction time τ_p for different normalized Rayleigh numbers R_a.
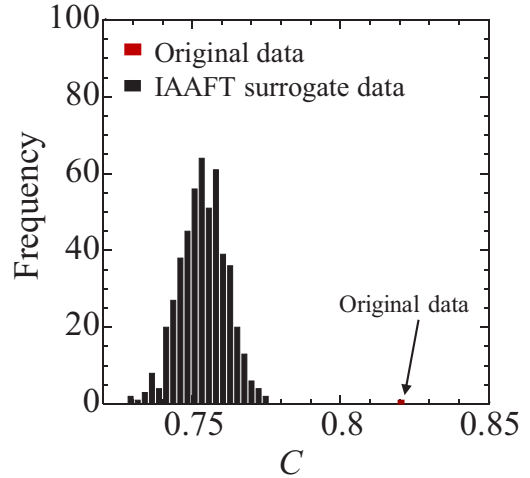

FIG. 11. Frequency distribution of correlation coefficient C for original and surrogate data at normalized Rayleigh number $R_a = -1$.

in Figs. 5–11 demonstrate that the flame front dynamics represents low (high)-dimensional deterministic chaos at $R_a > 0$ ($R_a < 0$).

We here discuss the physical mechanism for the increase in the randomness of the flame front dynamics at $R_a \leqslant 0$, focusing on the local maxima in H in terms of x. Note that the local maxima in H correspond to cusps in Ref. [9]. The temporal evolution of the local maxima in H in terms of x is shown in Fig. 12 for different R_a. A striped pattern with a relatively constant distance between flame wrinkles is clearly formed at $R_a = 0$, accompanying with the sudden appearance and disappearance of flame wrinkles. The local appearance and disappearance are attributed to the merging and dividing of contiguous wrinkles. The flame wrinkles interact continuously and randomly with each other with increasing g ($R_a < 0$), leading to the collapse of the striped pattern. This is an important feature of the strong nonlinear mutual interaction between multiple scales of wrinkles. The flame wrinkles merge and divide much faster with increasing g. It is interesting to note that a local order pattern at $\tau = 800$ emerges in the complex spatiotemporal structure during the nonlinear evolutions of flame wrinkles. Figure 13 shows the variations in the mean distance $\langle d \rangle$ between local maxima and the probability density function $P(\xi)$ of the normalized distance between local maxima at $R_a \leqslant 0$. Both $\langle d \rangle$ and $P(\xi)$ at $\xi > 1$ significantly increase with g. This indicates that the promotion of Rayleigh-Taylor instability in negative gravity gives rise to large-scale wrinkles on the flame front. Fernández-Galisteo *et al.* [37] have recently showed that for an upwardly propagating flame in a Hele-Shaw cell, the enhanced gravity significantly increases the propagation speed and flame surface area, resulting in an increase in the amplitude of flame wrinkles. The irregular formation of large-scale wrinkles plays an important role in the formation of high-dimensional deterministic chaos. This results in the increase in the randomness of flame front dynamics in a Hele-Shaw cell. In this work, we have derived a nonlinear evolution equation modeling flame front instability in a Hele-Shaw cell subjected to a buoyant force and have
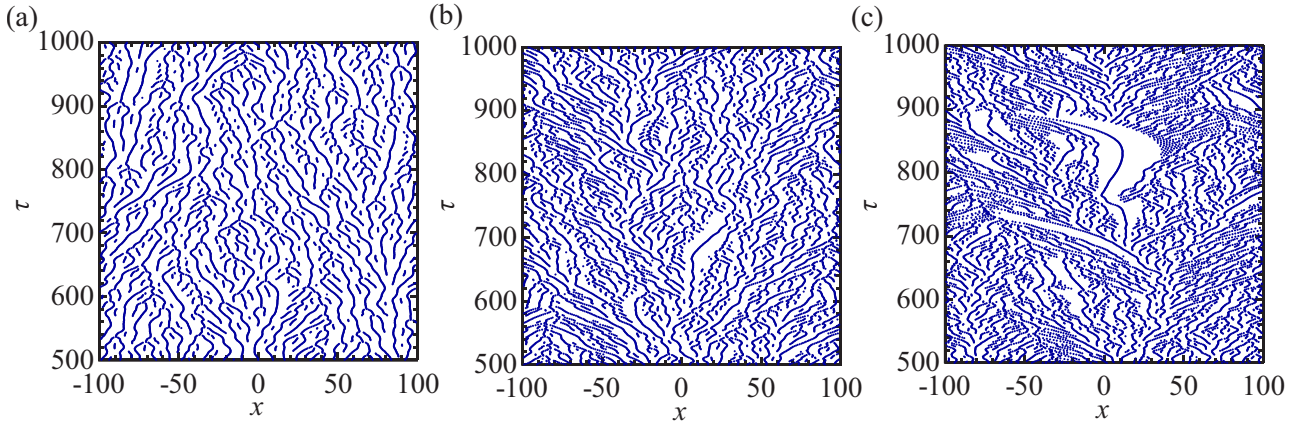
FIG. 12. Temporal evolution of local maxima in flame front fluctuations H in terms of location x for different normalized Rayleigh numbers R_a. (a) $R_a = 0$, (b) $R_a = -1$, and (c) $R_a = -2$.

focused on the characterization of spatiotemporal flame front dynamics under enhanced gravity. Our nonlinear evolution equation gives a comprehensive physical interpretation that is as simple as possible for the dynamical mechanism by which
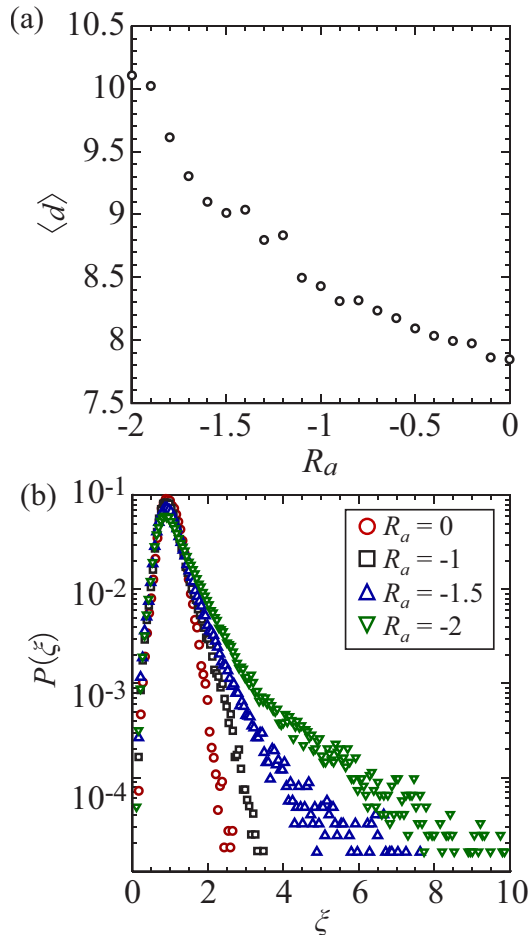

FIG. 13. Variations in (a) mean distance $\langle d \rangle$ between local maxima and (b) probability density function $P(\xi)$ of normalized distance between local maxima at normalized Rayleigh number $R_a \leqslant 0$.

deterministic chaos due to the interplay between hydrodynamic and thermal-diffusive effects is progressively promoted with increasing gravitational level at $R_a < 0$. The presence of low (high)-dimensional deterministic chaos at $R_a > 0$ ($R_a < 0$) in flame front dynamics was not elucidated in the previous studies using nonlinear evolution equations [4–7,35]. Our results are expected to provide a physical understanding of spatiotemporal flame front dynamics in a Hele-Shaw cell.

Finally, there is an important point concerning the analytical method we should include in our next study. We have demonstrated that the transition network entropy is a useful measure for capturing subtle changes in the randomness of flame front dynamics. The ordinal partition transition network we used in this study is constructed from the continuous signals of H. How can one more deeply understand the nonlinear mutual interaction between multiple scales of wrinkles in flame front from the viewpoint of complex networks? To this end, the temporal dynamics of a spatial network consisting of discrete signals, that is, the local maxima of H, will be examined in our next study.

V. SUMMARY

We have studied the effect of gravity on spatiotemporal flame front dynamics in a Hele-Shaw cell from the viewpoint of complex networks. A nonlinear evolution equation is theoretically derived and numerically solved to produce flame front dynamics. The randomness in the flame front dynamics significantly increases (decreases) with increasing gravitational level when the normalized Rayleigh number R_a is negative (positive). This is clearly identified by two network entropies: the flame front network entropy estimated from the degree distribution in the natural visibility graph and the transition network entropy in the ordinal partition transition network. Low-dimensional deterministic chaos appears in the flame front dynamics at $R_a > 0$, which is satisfactorily shown by the permutation transition spectrum test, multiscale complexity-entropy causality plane, and nonlinear forecasting method. The formation of high-dimensional deterministic chaos becomes apparent with increasing gravitational level at $R_a < 0$. The irregular formation of large-scale wrinkles driven

by the Rayleigh-Taylor hydrodynamic instability plays an important role in promoting the formation of high-dimensional deterministic chaos at $R_a < 0$, resulting in the randomness of flame front dynamics.

[1] G. H. Markstein, *Nonsteady Flame Propagation* (MacMillan, New York, 1964).

[2] G. I. Sivashinsky, Combust. Sci. Tech. **15**, 137 (1977).

[3] L. D. Landau, Acta Phys. Chim. **19**, 77 (1944).

[4] G. I. Sivashinsky, Acta Astronaut. **4**, 1177 (1977).

[5] D. M. Michelson and G. I. Sivashinsky, Acta Astronaut. **4**, 1207 (1977).

[6] G. Joulin and P. Cambray, Combust. Sci. Tech. **81**, 243 (1992).

[7] F. Creta, N. Fogla, and M. Matalon, Combust. Theor. Model. **15**, 267 (2011).

[8] K. Mukaiyama, S. Shibayama, and K. Kuwana, Combust. Flame **160**, 2471 (2013).

[9] C. Almarcha, B. Radisson, E. Al Sarraf, E. Villermaux, B. Denet, and J. Quinard, Phys. Rev. E **98**, 030202(R) (2018).

[10] A-L. Barabási, *Network Science* (Cambridge University Press, Cambridge, 2016).

[11] K. Taira, A. G. Nair, and S. L. Brunton, J. Fluid Mech. **795**, R2 (2016).

[12] R. I. Sujith and V. R. Unni, Phys. Fluids **32**, 061401 (2020).

[13] G. Iacobello, L. Ridolfi, and S. Scarsoglio, Physica A **563**, 125476 (2021).

[14] L. Lacasa, B. Luque, F. Ballesteros, J. Luque, and J. C. Nuno, Proc. Natl. Acad. Sci. USA **105**, 4972 (2008).

[15] B. Luque, L. Lacasa, F. Ballesteros, and J. Luque, Phys. Rev. E **80**, 046103 (2009).

[16] R. V. Donner, M. Small, J. F. Donges, N. Marwan, Y. Zou, R. Xiang, and J. Kurths, Int. J. Bifur. Chaos **21**, 1019 (2011).

[17] J. Zhang and M. Small, Phys. Rev. Lett. **96**, 238701 (2006).

[18] Y. Okuno, M. Small, and H. Gotoda, Chaos **25**, 043107 (2015).

[19] M. Murugesan and R. I. Sujith, J. Fluid Mech. **772**, 225 (2015).

[20] V. Godavarthi, V. R. Unni, E. A. Gopalakrishnan, and R. I. Sujith, Chaos **27**, 063113 (2017).

[21] J. Singh, V. R. Belur, S. Chaudhuri, and R. I. Sujith, Chaos **27**, 043107 (2017).

[22] Y. Guan, L. K. B. Li, B. Ahn, and K. T. Kim, Chaos **29**, 053124 (2019).

[23] H. Kinugawa, K. Ueda, and H. Gotoda, Chaos **26**, 033104 (2016).

[24] H. Gotoda, H. Kobayashi, and K. Hayashi, Phys. Rev. E **95**, 022201 (2017).

[25] K. Takagi, H. Gotoda, I. T. Tokuda, and T. Miyano, Phys. Rev. E **96**, 052223 (2017).

[26] K. Takagi, H. Gotoda, I. T. Tokuda, and T. Miyano, Phys. Lett. A **382**, 3181 (2018).

[27] M. Small, Proc. IEEE Int. Symp. Circuits Syst., 2509 (2013).

[28] M. McCullough, M. Small, T. Stemler, and H. H.-C. Iu, Chaos **25**, 053101 (2015).

[29] C. Aoki, H. Gotoda, S. Yoshida, and S. Tachibana, J. Appl. Phys. **127**, 224903 (2020).

[30] N. Peters, *Turbulent Combustion* (Cambridge University Press, Cambridge, 2004).

[31] G. I. Sivashinsky and P. Clavin, Journal de Physique **48**, 193 (1987).

[32] Z. Rakib and G. I. Sivashinsky, Combust. Sci. Tech. **54**, 69 (1987).

[33] Z. Rakib and G. I. Sivashinsky, Combust. Sci. Tech. **59**, 247 (1988).

[34] G. I. Sivashinsky, C. K. Law, and G. Joulin, Combust. Sci. Tech. **28**, 155 (1982).

[35] K. Kuwana, Nagare **31**, 357 (2012) (in Japanese).

[36] P. M. Vilela and D. A. Vasquez, Chaos **24**, 023135 (2014).

[37] D. Fernández-Galisteo, V. N. Kurdyumov, and P. D. Ronney, Combust. Flame **190**, 133 (2018).

[38] D. Fernández-Galisteo and V. N. Kurdyumov, Proc. Combust. Inst. **37**, 1937 (2019).

[39] D. Elliott and D. A. Vasquez, Phys. Rev. E **85**, 016207 (2012).

[40] H. Gotoda, M. Pradas, and S. Kalliadasis, Phys. Rev. Fluids **2**, 124401 (2017).

[41] A. Kassam and L. N. Trefethen, SIAM J. Sci. Computing **26**, 1214 (2005).

[42] C. Bandt and B. Pompe, Phys. Rev. Lett. **88**, 174102 (2002).

[43] C. W. Kulp and L. Zunino, Chaos **24**, 033116 (2014).

[44] W. Kobayashi, H. Gotoda, S. Kandani, Y. Ohmichi, and S. Matsuyama, Chaos **29**, 123110 (2019).

[45] F. Olivares, M. Zanin, L. Zunino, and D. G. Pérez, Chaos **30**, 063101 (2020).

[46] T. Schreiber and A. Schmitz, Phys. Rev. Lett. **77**, 635 (1996).

[47] L. Zunino, M. C. Soriano, and O. A. Rosso, Phys. Rev. E **86**, 046210 (2012).

[48] Y. Tang, A. Zhao, Y. Y. Ren, F. X. Dou, and N. D. Jin, Physica A **449**, 324 (2016).

[49] Y. Z. Wang, J. Singer, and H. H. Bau, J. Fluid Mech. **237**, 479 (1992).

[50] C. Tong and A. Gluhovsky, Phys. Rev. E **65**, 046306 (2002).

[51] F. F. Araujo, S. Grossmann, and D. Lohse, Phys. Rev. Lett. **95**, 084502 (2005).

[52] W. M. Macek and M. Strumik, Phys. Rev. E **82**, 027301 (2010).

[53] M. T. Rosenstein, J. J. Collins, and C. J. D. Luca, Physica D **65**, 117 (1993).

[54] A. Jayaraman, J. D. Scheel, H. S. Greenside, and P. F. Fischer, Phys. Rev. E **74**, 016209 (2006).

[55] H. Gotoda, Y. Shinoda, M. Kobayashi, Y. Okuno, and S. Tachibana, Phys. Rev. E **89**, 022910 (2014).

[56] H. Gotoda, Y. Okuno, K. Hayashi, and S. Tachibana, Phys. Rev. E **92**, 052906 (2015).